Particuology 115 (2026) 214–227

Contents lists available at ScienceDirect

Particuology

journal homepage: www.elsevier.com/locate/partic

Numerical simulation of plastic pyrolysis in fluidized bed reactors under continuous and batch-wise feeding

Muhao Li[a], Feichi Zhang[a,*], Thorsten Zirwes[b], Oliver T. Stein[c], Salar Tavakkol[a,**], Dieter Stapf[a]

[a] Institute for Technical Chemistry (ITC), Karlsruhe Institute of Technology (KIT), Kaiserstr.12, 76131, Karlsruhe, Germany
[b] Institute for Reactive Flows, University of Stuttgart, Pfaffenwaldring 31, 70569, Stuttgart, Germany
[c] Engler-Bunte-Institute (EBI), Division for Combustion Technology, Karlsruhe Institute of Technology (KIT), Engler-Bunte-Ring 7, 76131, Karlsruhe, Germany

HIGHLIGHTS

- Eulerian–Lagrangian CFD solver developed for plastic pyrolysis in fluidized bed reactors.
- Lumped kinetics and particle-scale heat transfer integrated for product yield prediction.
- Baseline modeling framework for plastic pyrolysis in fluidized bed reactors.
- Stronger thermal inhomogeneity during the first 10 s for batch-wise feeding.
- Similar final product selectivity for both batch-wise and continuous feeding.

GRAPHICAL ABSTRACT

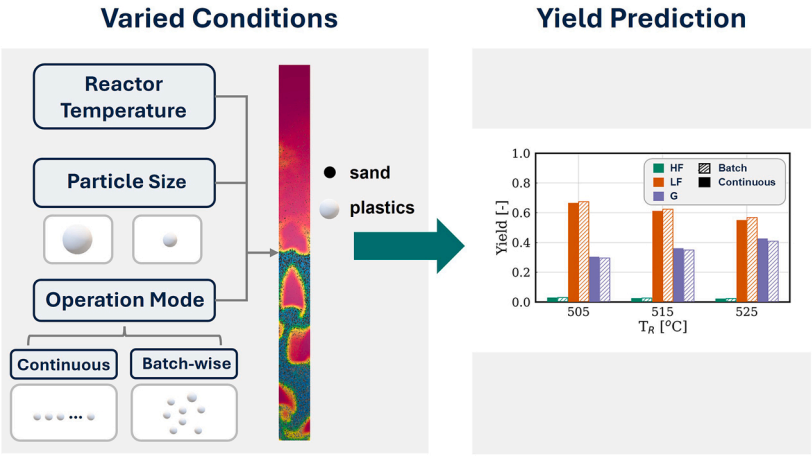

ARTICLE INFO

Keywords:
Eulerian–Lagrangian
Plastic pyrolysis
Fluidized bed reactor
Chemical recycling

ABSTRACT

Numerical simulations were conducted to study the pyrolysis of polypropylene (PP) in a fluidized bed reactor (FBR). For that purpose, a Eulerian–Lagrangian solver was developed, incorporating the gas–solid hydrodynamics in FBR, particle-level heat transfer, and a five-lump pyrolysis reaction kinetic model. This framework captures the mutual interplay among these physicochemical processes and enables predicting the yields of permanent gas (G), light fraction (LF), and heavy fraction (HF). Analysis of the characteristic timescales confirms that the pyrolysis reaction is significantly slower than convective heat transfer. At 505 °C, LF was the dominant product (67.4 wt%), followed by G (29.6 wt%) and HF (3 wt%), and the product distribution significantly shifted toward G formation with increasing reactor temperature. In contrast, variations in particle size (1.5–2.5 mm) and

This article is part of a special issue entitled: Reactive Particle-Gas Systems II published in Particuology.

* Corresponding author.
** Corresponding author.
E-mail addresses: feichi.zhang@kit.edu (F. Zhang), salar.tavakkol@kit.edu (S. Tavakkol).

https://doi.org/10.1016/j.partic.2026.05.017
Received 29 November 2025; Received in revised form 7 May 2026; Accepted 25 May 2026
Available online 1 June 2026

operation mode (batch-wise vs. continuous) affected the transient thermal behavior but had minor effects on product yields, as heat transfer is not rate-determining under the investigated conditions.

1. Introduction

Due to the widespread use of plastics, global plastic waste generation has risen sharply. In 2019, approximately 353 Mt of plastic waste was generated worldwide, with roughly 70 % either landfilled or incinerated, and around 20 % leaking into the environment due to improper management, causing severe environmental issues such as microplastic pollution (OECD, 2022). While mechanical recycling is more effective for pure plastic waste, chemical recycling enables the treatment of mixed and contaminated plastic waste. Among the current chemical-recycling technologies, pyrolysis offers the best balance between investment cost, operating cost and product quality compared to gasification and hydrothermal liquefaction (Dai et al., 2022; Dogu et al., 2021). Moreover, because of superior heat transfer characteristics, fluidized bed reactors (FBR) have been widely employed in plastic pyrolysis research.

During the pyrolysis process, plastic waste is decomposed in a high-temperature, oxygen-free environment into shorter-chain molecules through a free-radical mechanism. The typical products include permanent gas (C_1 – C_4), pyrolysis oil with a wide carbon-number distribution (up to approximately C_{35}), and, depending on the feedstock, possible solid residues. Owing to its chemical similarity to crude-oil-derived feedstocks, pyrolysis oil has strong potential as a surrogate feedstock in chemical processes such as steam cracking, where it can be further converted into light olefins for producing new plastics (Kusenberg et al., 2022). Therefore, predicting and optimizing product yields, e.g. increasing the fraction of light paraffin within the naphtha range to meet the requirements of the steam-cracking industry, constitute key objectives in experimental investigations.

The experimental investigation of plastic pyrolysis began in the 1950s (Madorsky, 1952, 1953), with fundamental insights initially obtained from milligram-scale laboratory experiments. Bockhorn et al. studied the degradation behavior of polyethylene (PE), polypropylene (PP) (Bockhorn, Hornung, Hornung, et al., 1999), and polyvinyl chloride (PVC) (Bockhorn, Hornung, & Hornung, 1999) using thermogravimetric analysis (TGA) and a gradient-free reactor, where global kinetic parameters were determined, and, through the integration of an online mass spectrometer (MS), detailed insights into product yields were achieved. To advance toward industrial application, larger-scale reactors at the kilogram scale were subsequently employed, among which FBRs and conical spouted bed reactors (CSBRs) were most widely used. Kaminsky et al. (2004) reported the pyrolysis of polymethyl methacrylate (PMMA) in a FBR, achieving a monomer yield exceeding 98 %. Another polymer suitable for monomer recovery is polystyrene (PS) (Merkel et al., 2023). Artetxe et al. (2015) performed pyrolysis of PS in a CSBR and obtained up to 70.5 wt% styrene. However, when polyolefins are used as feedstock, the resulting products are typically mixtures of gas, liquid, and wax with a broad carbon-number distribution (C_1 – C_{30+}), which cannot be directly reused without further upgrading (Elordi et al., 2011). To increase the yield of light olefins (monomers), catalytic pyrolysis has been widely investigated, with catalysts applied either in-situ within the reactors (Donaj et al., 2012; Netsch et al., 2023) or ex-situ in a downstream fixed bed (Artetxe et al., 2012). However, catalyst deactivation remains a major challenge. Consequently, a more practical approach is to employ pyrolysis oil as an alternative feedstock for steam cracking. The key issue that still needs to be addressed is the higher olefin and aromatic content, along with a broader boiling range compared with petroleum-derived feedstocks (Kusenberg et al., 2022). Besides these developments, the operation mode emerged as another key parameter for industrial viability, involving a shift from batch-wise to continuous feeding to achieve higher throughput. Elordi et al. (2009) reported the continuous catalytic pyrolysis of high-density polyethylene (HDPE) in a CSBR at 1 kg/h. Demonstrating further scaling, Kaminsky (2021) reported FBRs capable of processing up to 50 kg/h plastic waste.

However, current experimental research remains largely limited to laboratory or pilot-scale. During scale-up, many interactions exhibit strong nonlinear behavior, making experimental exploration alone impractical and prohibitively expensive. Consequently, numerical simulation serves as an effective and economical tool to reveal underlying mechanisms and guide process optimization. Zhang et al. (2025) conducted particle-resolved computational fluid dynamic (CFD) simulations of HDPE particles with different shapes and sizes. They found that cylindrical particles exposed to longitudinal flow degraded more slowly than spherical ones, and that for particles larger than 4 mm, the thermally-thin assumption was no longer valid. The same research group (Zhang, Dai, et al., 2026) also employed full 3D Eulerian–Lagrangian simulations to systematically analyze the hydrodynamics of conical spouted beds. Mazloum and co-workers (Mazloum et al., 2021) simulated the heat transfer and melting behavior of plastics using the finite element method, where the melting effect was incorporated by adding the enthalpy of fusion to the heat capacity. The results showed good agreement with experimental data. Ding et al. (2020) performed a CFD simulation of solid-waste pyrolysis (primarily consisting of plastics and biomass) using an Eulerian–Eulerian approach, in which plastic degradation was represented by a single-step kinetic model. Similarly, De la Flor-Barriga and Rodríguez-Zúñiga (2022) simulated the catalytic pyrolysis of HDPE in a two-dimensional FBR using an Eulerian–Eulerian approach, but incorporating a multistep kinetic scheme. Shen et al. (2024, 2025) performed a CFD–DEM simulation of HDPE pyrolysis in an FBR, integrating a neural network-inspired kinetic model, in which the pyrolysis process was divided into melt-phase and gas-phase reactions. The simulation results showed good agreement with experimental measurements.

As discussed above, most CFD simulations of plastic pyrolysis utilized the Eulerian–Eulerian approach, which cannot resolve particle-scale phenomena or examine their influence on product yields. Moreover, no simulation studies have compared the differences between batch-wise and continuous feeding. In this work, a Eulerian–Lagrangian CFD solver has been developed, which incorporates gas–solid multiphase flow, particle-level heat transfer, and a five-lump reaction kinetic model, enabling the prediction of product yields from plastic pyrolysis. The model has been applied to simulate a laboratory-scale FBR designed for plastic pyrolysis. Its predicted hydrodynamic behavior is first analyzed, followed by a detailed investigation of the pyrolysis process. Furthermore, the effects of reactor temperature, plastic particle size, and operation mode on product yields are systematically investigated, providing insights and guidance for process optimization.

2. Model description

The pyrolysis of plastics in an FBR involves complex physicochemical processes from the molecular to the reactor scale, as illustrated in Fig. 1. Plastic particles are fed into a preheated reactor at room temperature, where they undergo intensive collisions with (preheated) inert particles. Gas flowing through the particle bed supplies thermal and kinetic energy to the system, and the resulting gas–particle hydrodynamic interactions promote heat transfer through conduction, convection, and radiation. As the plastic particles heat up, intraparticle temperature gradients may develop due to their low thermal conductivity. At high enough temperatures, the plastic particles soften (in the case of amorphous plastics) or melt (for semi-crystalline polymers), forming a sticky, non-Newtonian fluid. At higher temperatures, pyrolysis reactions occur via a free-radical mechanism, in which backbone C–C bonds undergo

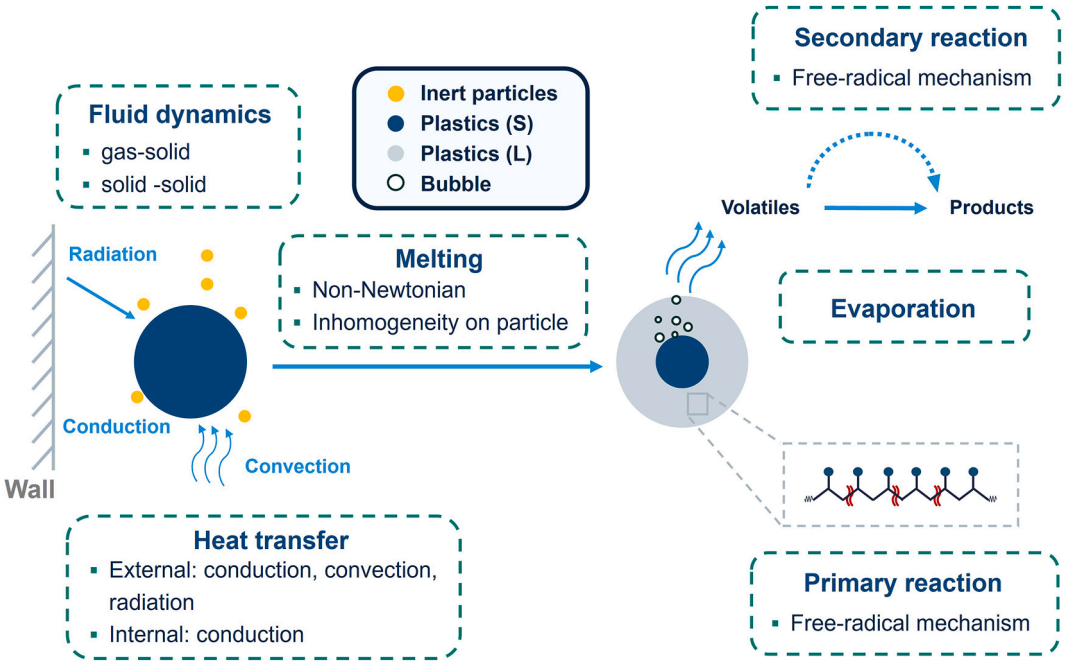

Fig. 1. Pyrolysis of plastics in FBRs.

random scission, H-abstraction and β-scission reactions, generating volatile short-chain molecules. These volatile species are subsequently released into the gas phase, carried upward by the fluidizing medium, and are ultimately condensed and collected as products. Secondary gas-phase reactions should also be considered at sufficiently long gas residence times.

In this work, a Eulerian–Lagrangian solver, incorporating four-way coupling, was employed to simulate the gas–solid multiphase flow. In the Eulerian–Lagrangian framework, the gas phase is treated as a continuum (Eulerian phase), while the solid phase is represented by discrete (Lagrangian) particles. Transport equations for mass, momentum, energy and species are solved for both phases, which are coupled through interphase source terms. The OpenFOAM solver `coalMPPICChemistryBuoyancyFoam` (Tavakkol et al., 2021) was modified to incorporate the newly developed submodels for interparticle collision forces, convective heat transfer, and reaction kinetics. The melting process has not been considered due to the lack of modeling approach for this effect. The plastic particles are tracked with the Lagrangian method, assuming a homogeneous temperature. The potential impact of neglecting the melting and intraparticle heat transfer will be discussed in Section 4.3.

2.1. Governing equations for the gas phase

In the Eulerian–Lagrangian approach, the gas phase dynamics are described by the transport equations for mass, momentum, energy, and species (Alobaid et al., 2022). The current model adopted the standard solver `coalChemistryFoam` in OpenFOAM to include four-way coupling and plastic pyrolysis kinetics. The point-particle approximation from the original solver is kept, which neglects the fluid volume displaced by particles in the Eulerian equations ($\epsilon \approx 1$). Discussion on the impacts of this adoption is detailed in Section 4.3.

2.1.1. Conservation of mass and momentum

The continuity and momentum equations for the variable-density gas phase are given by

$$\frac{\partial \rho_g}{\partial t} + \nabla\cdot(\rho_g \mathbf{U}_g) = S_\rho, \tag{1}$$

$$\frac{\partial(\rho_g \mathbf{U}_g)}{\partial t} + \nabla\cdot(\rho_g \mathbf{U}_g \mathbf{U}_g) = -\nabla p + \rho \mathbf{g} + \nabla\cdot\tau + \mathbf{S}_U, \tag{2}$$

where ρ_g, $\mathbf{U}_g$, and p are the density, velocity, and pressure of the gas phase, respectively. S_ρ is the mass source term from the particle phase (devolatilization). $\mathbf{S}_U$ represents the momentum exchange source term, primarily composed of the drag force exerted by the particles on the gas. The detailed representation of each source term in Eqs. (1)–(4) will be shown in Section 2.2. The stress tensor $\nabla \cdot \tau$ describes viscous forces acting on the fluid.

2.1.2. Energy transport

The transport of energy is derived based on the sensible enthalpy (h_s) of the system

$$\begin{aligned}&\frac{\partial(\rho_g h_s)}{\partial t} + \nabla\cdot(\rho_g \mathbf{U}_g h_s) + \frac{\partial(\rho_g K)}{\partial t} + \nabla\cdot(\rho_g \mathbf{U}_g K)\\ &= \frac{\partial p}{\partial t} + \nabla\cdot(\lambda_g \nabla T_g) + \rho_g \mathbf{U}_g\cdot g + \dot{q} + S_h,\end{aligned} \tag{3}$$

where $K = \frac{1}{2}|\mathbf{U}_g|^2$ is the specific kinetic energy, λ_g is the thermal conductivity of the gas phase, and $\dot{q}$ is the heat source from gas-phase reactions. Furthermore, S_h is the heat exchange with the particle phase.

2.1.3. Species transport

The gas phase consists of the inert fluidizing medium and the released volatile species, with the conservation equation for each gas-phase species i given by

$$\frac{\partial(\rho_g Y^i)}{\partial t} + \nabla\cdot(\rho_g \mathbf{U}_g Y^i) - \nabla\cdot(\rho_g\, D\, \nabla Y^i) = S_Y^i + r_g^i, \tag{4}$$

where Y^i is the mass fraction of species i and r_g^i its reaction rate in the gas phase, which is neglected here because the gas residence time is much shorter than the characteristic timescale of gas-phase reactions at around 500 °C (for reference, less than a 30 % compositional change occurs at 750 °C within a gas residence time of 4 s (van Wyk et al., 2026)). S_Y^i represents the contribution from particle-phase devolatilization, which is formed from the particle-phase primary pyrolysis

reaction. The details of the (particle-phase) reaction kinetics are presented in Section 2.3.

2.2. Governing equations of the particle phase

In contrast to the Eulerian gas phase, the particle phase is treated in a Lagrangian framework, where each computational parcel represents a group of particles and evolves according to a set of ordinary differential equations. Sand and plastic particles are defined within the same Lagrangian phase, with the (inert) sand and (active) plastic particles share same submodels expect for pyrolysis reactions.

To clearly distinguish the different particle types and their respective components, the following notation is adopted throughout this work: subscripts denote the phase and identity of the material, where p refers to the Lagrangian particle phase, further specified as p, sand for sand particles and p, pl for plastic particles, while g denotes the Eulerian gas phase.

2.2.1. Mass balance

As mentioned at the beginning of Section 2, the mass of plastic particles $m_{p,\mathrm{pl}}$ decreases during pyrolysis due to devolatilization, governed by

$$\frac{\mathrm{d}m_{p,\mathrm{pl}}}{\mathrm{d}t} = -\sum_{i\in V} r^i_{\mathrm{dev}}, \tag{5}$$

where r^i_{dev} is the devolatilization rate of volatile component i, and V is the set of all volatile species. As will be explained in Section 2.3, the volatile components are assumed to be immediately released into the gas phase upon their formation, which means that their devolatilization rate r^i_{dev} is identical to the formation rate r^i. Therefore, Eq. (5) can be rewritten as

$$\frac{\mathrm{d}m_{p,\mathrm{pl}}}{\mathrm{d}t} = -\sum_{i\in V} r^i_{\mathrm{dev}} = -\sum_{i\in V} r^i. \tag{6}$$

This mass loss serves as the mass source S_ρ in the Eulerian gas-phase continuity equation (Eq. (1)). By averaging the contributions from all N_p, pl particles within a computational cell of volume V_{cell}, we obtain

$$S_\rho = \frac{1}{V_{\mathrm{cell}}} \cdot \sum_{n=1}^{N_{p,\mathrm{pl}}} \left(\sum_{i\in V} r^i \right)_n. \tag{7}$$

The reaction source term is only active for the plastic particles, an internal check for inert components is implemented to bypass solving the reaction equations for sand particles.

2.2.2. Momentum balance

The trajectory and velocity $\mathbf{U}_p$ of each particle are described by Newton's second law

$$m_p \frac{\mathrm{d}\mathbf{U}_p}{\mathrm{d}t} = \sum_i \mathbf{F}_i = \mathbf{F}_c + \mathbf{F}_d + \mathbf{F}_g, \tag{8}$$

where the forces considered are gravity and buoyancy ($\mathbf{F}_g$), gas–particle drag ($\mathbf{F}_d$), and interparticle collision forces ($\mathbf{F}_c$).

The gravity term $\mathbf{F}_g$, including buoyancy, is expressed as

$$\mathbf{F}_g = m_p \cdot \mathbf{g} \cdot \left(1 - \frac{\rho_g}{\rho_p}\right). \tag{9}$$

The drag force $\mathbf{F}_d$ is calculated using the Gidaspow drag model (Gidaspow, 1994), which applies the Ergun equation and the Wen–Yu equation in different ranges of void fraction ϵ

$$|\mathbf{F}_d| = \begin{cases} \left(150\ \dfrac{1-\epsilon}{\epsilon} + 1.75\ Re_p\right) \dfrac{(1-\epsilon)\ \mu_g}{d_p^2} & \epsilon < 0.8 \\ \dfrac{3}{4}\ C_d\ \dfrac{(1-\epsilon)\ \epsilon^{-1.65}\ \mu_g\ Re_p}{d_p^2} & \epsilon \geq 0.8 \end{cases} \tag{10}$$

Here, $Re_p = (\rho_g |\mathbf{U}_g - \mathbf{U}_p| d_p)/\mu_g$ is the particle Reynolds number, C_d is the particle drag coefficient, and void fraction $\epsilon = V_g/V_{\mathrm{cell}}$ is the volume fraction of gas in each computational cell.

The interparticle collision force $\mathbf{F}_c$ is modeled using the Multiphase Particle-in-Cell (MP-PIC) approach (Andrews & O'Rourke, 1996), where $\mathbf{F}_c$ is derived from the spatial gradient of the particle stress τ_p, expressed as

$$\mathbf{F}_c = -m_p \frac{\nabla \tau_p}{(1-\epsilon)\ \rho_p} = -\frac{\pi\ d_p^3}{6\ (1-\epsilon)}\ \nabla \tau_p, \tag{11}$$

where the particle stress τ_p is evaluated based on the local solid volume fraction using the model proposed by Harris and Crighton (1994). Since sand and plastic particles are defined within the same Lagrangian phase, this formulation inherently accounts for collisions both among particles of the same type and between sand and plastic particles.

Consequently, the source term S_U in Eq. (2) is calculated from

$$S_U = \frac{1}{V_{\mathrm{cell}}} \cdot \sum_{n=1}^{N_p} \left[F_d + \frac{\Delta m_p}{\Delta t}\ \mathbf{U}_p \right]_n. \tag{12}$$

2.2.3. Energy balance

Each particle in the FBR exchanges energy with surrounding particles and the gas phase through conduction, convection, and radiation. Furthermore, for reactive particles (i.e., plastic particles), thermochemical effects must also be taken into account with

$$m_p\ c_{p,p}\ \frac{\mathrm{d}T_p}{\mathrm{d}t} = Q_{\mathrm{conv}} + Q_{\mathrm{cond}} + Q_{\mathrm{rad}} + Q_R, \tag{13}$$

where $c_{p,p}$ is the specific heat capacity of the particle p and the terms on the right-hand side represent convective, conductive, and radiative heat transfer, as well as the thermochemical effects associated with the pyrolysis reactions.

The convective heat transfer Q_{conv} is calculated from

$$Q_{\mathrm{conv}} = h\ A_p\ (T_g - T_p) = \frac{Nu\ \lambda_g}{d_p}\ A_p\ (T_g - T_p), \tag{14}$$

where h is the heat transfer coefficient, A_p is the particle surface area, λ_g is the thermal conductivity of the gas phase, and d_p is the particle diameter. The Nusselt number $Nu = h\ d_p/\lambda_g$ is determined using Gunn's correlation (Gunn, 1978), which accounts for the local void fraction ϵ

$$\begin{aligned} Nu = {} & (7 - 10\epsilon + 5\epsilon^2)(1 + 0.7\ Re_p^{0.2}\ Pr^{1/3}) \\ & + (1.33 - 2.4\epsilon + 1.2\epsilon^2)\ Re_p^{0.7}\ Pr^{1/3}, \end{aligned} \tag{15}$$

where $Pr = \mu_g c_{p,g}/\lambda_g$ is the Prandtl number. Eq. (15) implicitly accounts for interparticle conductive heat transfer via ϵ, leading to enhanced heat transfer (higher Nu) in regions with higher solid volume fraction (lower ϵ).

Furthermore, since the reactor temperature is relatively low (at around 500 °C), radiative heat transfer Q_{rad} is also neglected (Oka, 2004). The last term Q_R represents the combined thermal effects of reaction enthalpy and evaporation. Since measuring the enthalpy of each reaction separately is difficult, particularly for reactions involving pseudo-species and occurring simultaneously with evaporation, the global enthalpy h_R measured by differential scanning calorimetry (DSC) in our previous work (Netsch et al., 2024) was employed

$$Q_R = -h_R \frac{\mathrm{d}m_{p,\mathrm{pl}}}{\mathrm{d}t} = h_R \sum_{i\in V} r^i. \tag{16}$$

The gas phase energy source term, S_h (Eq. (3)), includes the heat exchanged with other particles and the sensible enthalpy carried by the released volatiles

$$S_h = \frac{1}{V_{\text{cell}}} \cdot \sum_{n=1}^{N_p} \left[-Q_{\text{conv}} + \sum_{i \in V} (r^i h_s^i(T_p)) \right]_n . \tag{17}$$

2.2.4. Species balance

As will be detailed in Section 2.3, the species are classified in two groups: low-boiling (i) and high-boiling (j) species. Due to relatively high boiling point, the unreacted polypropylene (PP) and wax (W) are assumed to be the only species in the particle phase, the mass evolution of which (solely caused by their l corresponding reactions) is governed by

$$\frac{\mathrm{d}m^j_{p,\,\text{pl}}}{\mathrm{d}t} = -\sum_l (r^j)_l . \tag{18}$$

In contrast, the volatile species $i \in V$ are assumed to be immediately released. Their formation rates r^i directly contribute to the gas-phase species source term S^i_Y in Eq. (4):

$$S^i_Y = \frac{1}{V_{\text{cell}}} \sum_{n=1}^{N_{p,\text{pl}}} (r^i)_n . \tag{19}$$

2.3. Reaction kinetics

A five-lump reaction kinetic model adopted from (Lechleitner et al., 2020) was employed to describe polypropylene (PP) pyrolysis, as illustrated in Fig. 2. Here, each "lump" represents a pseudo-species with a specific boiling-point range, which is a common simplification in petrochemical research that allows convenient and computationally efficient kinetic modeling (de Oliveira et al., 2016).

In this model, the degradation of PP begins with the formation of long-chained intermediates, wax (W), which subsequently decompose into heavy fraction (HF) (vacuum-gas-oil-like), light fraction (LF) (naphtha- and kerosine-like) and permanent gas (G). The original kinetic formulation modeled the degradation within a "quasi-homogeneous" bulk phase, i.e., evaluating the species mass fractions based on total mass, without specifying the distribution of species in gas or particle phases. To adapt this kinetics for the present multiphase simulation, explicit phase-partitioning assumptions are introduced. Since the boiling points of HF, LF and G are far below the reactor temperature, they were assumed to be instantaneously released into the gas phase upon formation. In contrast, although the intermediate W could theoretically partition between the gas and particle phases under the investigated conditions, it is allocated solely to the particle phase to simplify the interphase mass transfer calculations. Furthermore, due to the short gas-phase residence time (2–4 s), subsequent reactions of these volatile products were neglected. The kinetic model is governed by the following equations:

$$\frac{\mathrm{d}m^{\text{P}}_{p,\text{pl}}}{\mathrm{d}t} = -k_0 \cdot m^{\text{P}}_{p,\text{pl}}, \tag{20}$$

$$\frac{\mathrm{d}m^{\text{W}}_{p,\text{pl}}}{\mathrm{d}t} = k_0 \cdot m^{\text{P}}_{p,\text{pl}} - k_1 \cdot m^{\text{W}}_{p,\text{pl}} - k_2 \cdot m^{\text{W}}_{p,\text{pl}} - k_3 \cdot m^{\text{W}}_{p,\text{pl}}, \tag{21}$$

$$\frac{\mathrm{d}m^{\text{HF}}_{g}}{\mathrm{d}t} = k_1 \cdot m^{\text{W}}_{p,\text{pl}}, \tag{22}$$

$$\frac{\mathrm{d}m^{\text{LF}}_{g}}{\mathrm{d}t} = k_2 \cdot m^{\text{W}}_{p,\text{pl}}, \tag{23}$$

$$\frac{\mathrm{d}m^{\text{G}}_{g}}{\mathrm{d}t} = k_3 \cdot m^{\text{W}}_{p,\text{pl}}, \tag{24}$$

where the rate constants k follow the Arrhenius law:

$$k = A \exp\left(-\frac{E_a}{RT} \right). \tag{25}$$

3. Simulation setups

3.1. Computational domain and grid

In the present work, a laboratory-scale cylindrical FBR with a diameter of 5 cm and a height of 60 cm was simulated. As shown in Fig. 3 (a) and (b), the computational mesh consisted of cubic cells with dimensions of 4 × 4 × 4 mm. The lower and upper boundaries represent the reactor inlet and outlet, respectively, through which the fluidizing gas enters the reactor and carries the volatile products, while the side wall is assumed non-transmissive and adiabatic. Since the pyrolysis can last for tens of minutes and simulating the full three-dimensional FBR for only a few seconds of fluid-dynamic behavior can require about one day of simulation time (Zhang et al., 2024), the original cylindrical computational domain was simplified to a single-cell-layer thin slice with a width of 5 cm, corresponding to the reactor diameter. In this configuration, gas motion was restricted to two dimensions, while particle dynamics remained three-dimensional. The quasi-2D setup is a commonly adopted approach in FBR modeling, especially when laminar gas flow is employ (Grace et al., 2020). To evaluate the accuracy, a dedicated validation was also conducted by comparing the predicted hydrodynamic behavior against experiments, showing good agreement with measured pressure drop and bed height.

At the beginning of the simulation, approximately 480,000 quartz

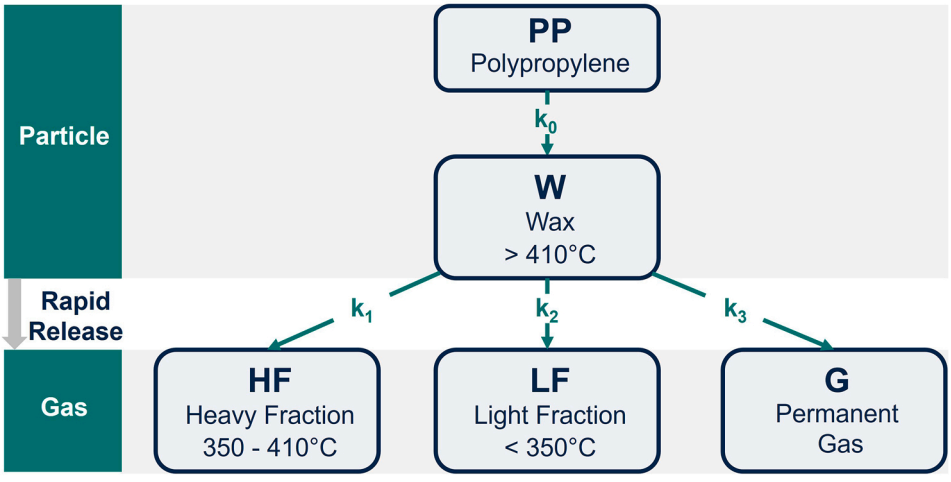

Fig. 2. Five-lump reaction kinetic model for PP (adapted from (Lechleitner et al., 2020)).

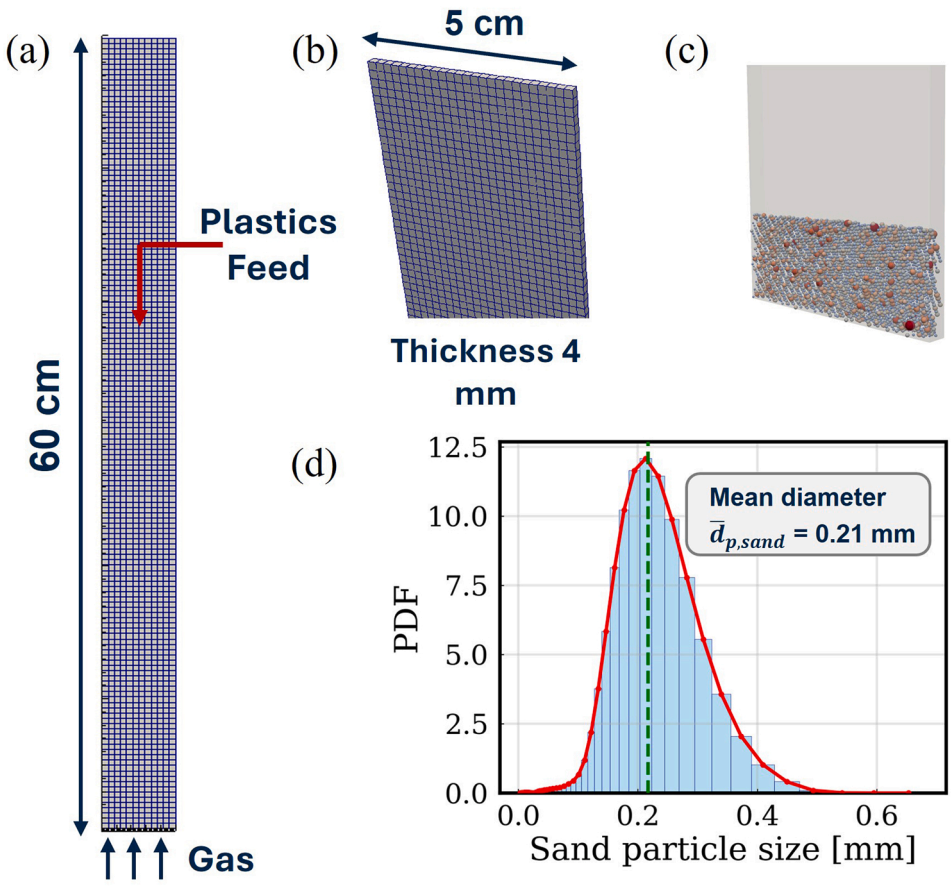

Fig. 3. Reactor geometry and initial position of sand particles.

sand particles (4 particles per parcel) with a total mass of 69.5 g and a Sauter mean diameter of 0.21 mm are introduced into the reactor and fluidized by the upward gas flow from the bottom of the reactor. After 0.5–1 s, a stable bubbling fluidized bed was formed. Plastic particles (1 particle per parcel) were then injected at a height of 45 cm, corresponding to the freeboard region, where they rapidly mix with the sand particles.

The numerical setup has been validated against cold-model experiments in our previous work (Zhang et al., 2024) in terms of the bed height and pressure drop under varied operating conditions. The validated setup was then employed to model plastic pyrolysis, incorporating both heat transfer and chemical reactions.

3.2. Material properties

Quartz sand is selected as the bed material, with its particle size distribution (PSD) shown in Fig. 3(d). The distribution is obtained from laser diffraction (Zhang et al., 2024). Methane (CH_4) is used as the fluidizing gas, as separating conventional inert gases such as N_2 from the product stream would require additional energy. Moreover, CH_4 is both a component of the gaseous product and inert under the investigated conditions. PP (Moplen HP 552H) was used as the feedstock.

The physicochemical properties of all materials are summarized in Table 1. For quartz sand, constant values of heat capacity and density are used. For CH_4, the default OpenFOAM material data are applied, where the transport properties are calculated using the Sutherland model, the heat capacity is obtained from the JANAF model, and the density is determined from the ideal gas law. The values listed in the table are evaluated over 25–550 °C. The density of PP is provided by the manufacturer, while its heat capacity was determined in our previous work (Netsch et al., 2024) using DSC and expressed as a piecewise linear function of temperature. Similar to CH_4, the properties of PP in the temperature range of 25–550 °C are presented in the table. For the intermediate species W, the density of PP is used due to difficulties in the measurement, and its heat capacity is calculated by using the representative species $C_{36}H_{74}$ (Durupt et al., 1996). Furthermore, the properties of volatile species (HF, LF and G) are assumed identical to CH_4, as their fractions are small compared with the inert gas.

Table 1
Summary of physicochemical properties.

Material	ρ (kg/m^3)	c_p (J/kg·K)	μ (10^{-5} Pa·s)	λ (mW/m·K)
Sand	2660	830	-	-
CH_4	0.237–0.656	2203.3–4301.6	1.84–3.97	57.7–234.9
PP	900	2238.4–3863.2	-	-
W	900	2248.9–3385.7	-	-
HF, LF, G	0.237–0.656	2203.3–4301.6	1.84–3.97	57.7–234.9

The kinetic parameters for the reaction pathways shown in Fig. 2 are listed in Table 2, adopted from the work of Lechleitner et al. (2020). However, since the reaction enthalpies in that study were estimated using approximate average enthalpies of formation, we instead use the overall apparent enthalpy of 542 kJ/kg determined experimentally via

Table 2
Summary of kinetic parameters.

Reaction	A (s^{-1})	E_a (kJ/mol)	h_R (kJ/kg)
0: PP → W	3.2×10^{15}	244	0
1: W → HF	2.0×10^{2}	80	542
2: W → LF	1.0×10^{5}	100	542
3: W → G	5.0×10^{14}	249	542

DSC in (Netsch et al., 2024). This value encompasses both pyrolysis reactions and evaporation. Because the exact composition of the lumped species and consequently, the specific intermediate steps involved are unclear, the partition of this value to each individual reaction is challenging. Therefore, a simplified implementation is adopted: the reaction enthalpy is coupled to the total particle mass loss from the three W-consuming reactions (Reactions 1–3), while the PP → W step is treated as thermally neutral.

3.3. Operating parameters

Both batch-wise and continuous feeding of the plastics are studied and compared. The study begins with batch-wise feeding, using pure CH_4 as the fluidizing gas with a superficial velocity of $U_g = 0.212$ m/s at a pressure of 1 atm. The target reactor temperature T_R is set to 505 °C, which falls within the typical temperature range for polyolefin pyrolysis (450–600 °C (Lopez et al., 2017)). Here, T_R is defined as the (quasi-) thermal equilibrium temperature of sand bed, more specifically, corresponding to the temperature immediately after mixing with plastics under batch-wise operation (at $t \approx 10$ s) or the steady-state temperature under continuous operation. At $t = 1$ s, 1.39 g of plastic particles (2 wt% of sand) with an initial temperature of 25 °C and a diameter of 2 mm are introduced into the reactor. To compensate for the rapid cooling caused by the introduction of cold plastic particles, the initially sand temperature $T_{p,\mathrm{sand},0}$ is set to an elevated, pre-calculated temperature. For instance, achieving $T_R = 505$, 515, and 525 °C requires initial gas inlet temperatures of $T_{g,\mathrm{in}} = 540$, 550, and 561 °C, respectively, with the sand pre-heated to the same temperature. The investigation of batch-wise operation continues with parameter study of both T_R and the plastic particle diameter $d_{p,\mathrm{pl}}$, with the focus on their effects on product yield. The boundary and initial conditions are listed in Table 3, and the simulation cases are summarized in Table 4.

For the gas phase, a no-slip condition is applied at the walls, which are treated as adiabatic. At the outlet, an open boundary condition is imposed on the velocity field to allow backflow, and a zero-gradient condition is applied to the temperature. For the particle phase, all walls are modeled with a rebound condition using a restitution coefficient of $e = 0.97$ and a friction coefficient of $\mu = 0.09$. The gas flow is treated as laminar because both the bulk gas ($Re_g = \rho_g \mathbf{U}_g D/\mu_g$) and particle Reynolds numbers (Re_p) are below 100 under the investigated conditions. This assumption was further verified through a supplementary simulation employing a Large Eddy Simulation (LES) turbulence model under identical conditions, which yields only negligible differences compared to the laminar flow results.

Subsequently, plastic particles are fed continuously at rates of $\dot{m}_{p,\mathrm{pl}} = 0.0234$, 0.0309, and 0.0408 g/s for $T_R = 505$, 515, and 525 °C, respectively. The primary challenge in setting up the continuous-feeding simulation lay in identifying the precise combination of initial and boundary conditions required for the system to reach a steady state. Preliminary energy and mass balance calculations were performed to estimate the required gas inlet temperature (set as constant), which determines the heat supplied for the pyrolysis. However, the steady-state heat input derived from these balances proved excessively high during the initial stage of the simulation. Because the steady-state plastic inventory is not yet reached and consequently energy consumption in the reactor is relatively low. Therefore, the excess heat continuously accumulated inside the reactor, causing the temperature to deviate from the target condition and preventing the system from reaching a steady state. The resulting gas inlet temperatures are considerably higher than in the batch cases, ranging from 624 to 747 °C, while the initial sand temperatures are set slightly below the target T_R to compensate for the continuous heat input (as shown in Table 4).

Table 3
Boundary and initial conditions.

Location	Variable	Condition
Gas phase		
Inlet	U_g	0.212 m/s (superficial)
Inlet	$T_{g,\mathrm{in}}$	Case-dependent (Table 4)
Inlet	Composition	Pure CH_4
Outlet	U_g	Open boundary
Outlet	T_g	Zero gradient
Walls	U_g	No-slip
Walls	T_g	Adiabatic
Particle phase		
All walls	Collision	Rebound ($e = 0.97$, $\mu = 0.09$)
Initial conditions		
Sand	$T_{p,\mathrm{sand},0}$	Case-dependent (Table 4)
Plastic	$T_{p,\mathrm{pl},0}$	25 °C
Batch	$m_{p,\mathrm{pl},0}$	1.39 g (2 wt% of sand, at $t = 1$ s)
Continuous	$\dot{m}_{p,\mathrm{pl}}$	Case-dependent (Table 4)

Table 4
Summary of simulation cases.

No.	Mode	T_R (°C)	$d_{p,\mathrm{pl}}$ (mm)	$T_{g,\mathrm{in}}$ (°C)	$T_{p,\mathrm{sand},0}$ (°C)	$\dot{m}_{p,\mathrm{pl}}$ (g/s)
0	Batch	505	2	540	540	–
1	Batch	**515**	2	550	550	–
2	Batch	**525**	2	561	561	–
3	Batch	505	**1.5**	540	540	–
4	Batch	505	**2.5**	540	540	–
5	**Cont.**	505	2	624	500	0.0234
6	**Cont.**	**515**	2	677	510	0.0309
7	**Cont.**	**525**	2	747	520	0.0408

4. Results and discussion

4.1. Gas–solid flow

The void fraction distribution at $t = 0$–1 s for $T_R = 505$ °C and $d_{p,\mathrm{pl}} = 2$ mm is illustrated in Fig. 4. Gas enters the reactor from the bottom, forming bubbles that grow as they rise through the bed. During their upward motion, bubbles exert interphase drag forces that drive the surrounding particles. Upon reaching the top of the sand bed, the bubbles burst, entraining sand particles into the freeboard region. After reaching their highest point, the sand particles fall back into the bed, where they collide with other particles and are re-entrained by newly formed bubbles. Due to higher gas velocity in the central region and lower velocity near the wall, a macroscopic particle circulation develops from the center toward the side regions.

This continuous bubble motion generates vigorous particle mixing,

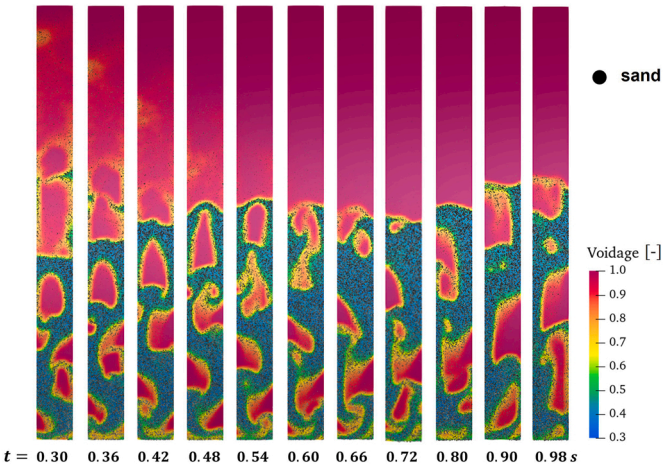

Fig. 4. Snapshots of calculated time series of void fraction distribution across the FBR.

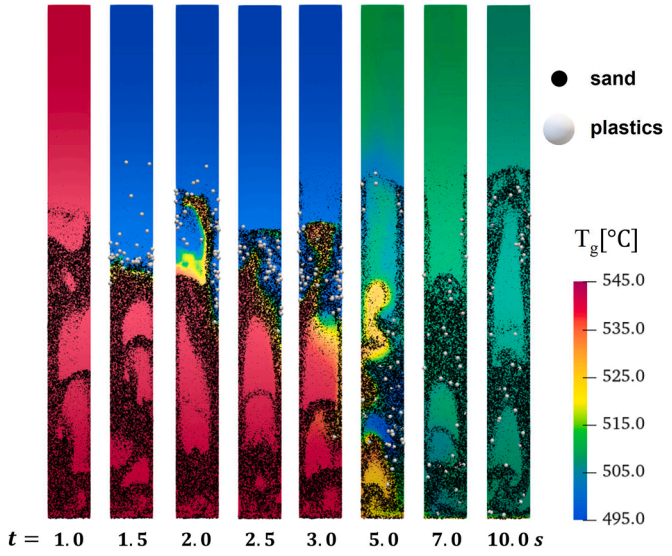

Fig. 5. Rapid particle mixing and temperature homogenization in the FBR.

as illustrated in Fig. 5. Here, the particle phase is colored and scaled by particle size, while the gas phase is colored by temperature. At $t = 1$ s, cold plastic particles (large white spheres) are injected, which then rapidly fall into the bed, causing a local cooling of the gas phase. Upon contacting the highly agitated sand bed, the plastic particles quickly mix with the smaller sand particles (small black spheres) within approximately 10 s. The vigorous bed agitation promotes extensive gas–solid contact, which significantly enhances convective heat transfer and drives a rapid homogenization of the gas temperature. Note that in both Figs. 4 and 5, the brightness gradient visible in the upper part of the column is a rendering effect introduced by ParaView's default Light Kit and does not reflect any physical temperature variation.

4.2. Pyrolysis reactions

Simulation results at $T_R = 505$ °C are shown in Fig. 6(a). As previously discussed, the vigorous mixing and agitation within the bed promote extensive gas–solid contact, thereby significantly enhancing convective heat transfer to the plastic particles. At $t = 10$ s, the plastic particles reach a thermal quasi-steady state, followed by the onset of the pyrolysis reaction. Here, the global conversion X, accounting for all plastic particles, is defined as

$$X = 1 - \frac{m_{p,\mathrm{pl}}}{m_{p,\mathrm{pl},0}} = 1 - \frac{m_{p,\mathrm{pl}}^{\mathrm{PP}} + m_{p,\mathrm{pl}}^{\mathrm{W}}}{m_{p,\mathrm{pl},0}}. \tag{26}$$

After approximately 200 s, the plastics are completely converted. A comparison between the heat-up period ($\overline{T}_p = 99.5\ \%\ \overline{T}_{p,\ \mathrm{end}}$) and the reaction period ($X = 99.5\%$) in Fig. 6(a) (red curve) clearly indicates that the pyrolysis reactions proceed significantly slower than external heat transfer. To quantitatively examine this relationship, the second Pyrolysis number is evaluated, defined as the ratio of the characteristic timescales of pyrolysis reactions and convective heat transfer (Pyle & Zaror, 1984)

$$Py_{II} \equiv \frac{\tau_{\mathrm{py}}}{\tau_{\mathrm{conv}}} = \frac{\frac{1}{k_{\mathrm{eff}}}}{\frac{\rho_{p,\mathrm{pl}} \cdot c_{p,p,\mathrm{pl}} \cdot R}{h}} = \frac{h}{\rho_{p,\mathrm{pl}} \cdot c_{p,p,\mathrm{pl}} \cdot R \cdot k_{\mathrm{eff}}}, \tag{27}$$

where $\rho_{p,\mathrm{pl}}$, $c_{p,p,\mathrm{pl}}$, and R are the density, specific heat, and radius of plastic particles, respectively. And k_{eff} is the effective rate constant of the lumped kinetic model at the operating temperature, calculated as

$$k_{\mathrm{eff}} = \frac{1}{\frac{1}{k_0} + \frac{1}{k_1 + k_2 + k_3}}. \tag{28}$$

Evaluation under the current operating conditions yields $Py_{II} = 6.15$, confirming that the characteristic time of pyrolysis is considerably larger than that of convective heating.

At the reactor outlet, the mass flow rates of HF, LF and G are recorded and integrated to determine product yields, as shown in Fig. 6(b). At $T_R = 505$ °C, LF is the main product with a yield of 67.4 wt%, followed by G (29.6 wt%) and HF (3 wt%). As previously mentioned, LF can serve as a surrogate feedstock of naphtha and kerosene in the petrochemical industry. Therefore, the impact of operating parameters will be discussed next with the aim of further enhancing LF yield.

4.2.1. Influence of reactor temperature

The impact of reactor temperature was investigated by increasing T_R by 10 and 20 °C. As shown in Fig. 7(a), all cases exhibit nearly identical heat-up periods, after which the average particle temperature stabilizes at levels corresponding to the respective T_R. With increasing T_R, LF yield decreases (from 67.4 to 56.7 wt%), while G production increases (from 29.6 to 40.9 wt%) and HF yield remains nearly constant (Fig. 7(b)). This trend can be explained from two perspectives. First, at higher temperatures, collisions among molecules and radicals occur more frequently, allowing more radicals to overcome the activation barrier and promoting C-C bond cleavage via β-scission. Second, among the three volatile-forming reactions (Table 2), W → G exhibits more than twice the activation energy of the others, making its rate most sensitive to temperature. Therefore, lower T_R favors LF formation.

Similar observations have been reported in experimental studies. Wong and Broadbelt (2001) conducted milligram-scale pyrolysis of PP in a sealed glass ampoule at 350 and 420 °C for 180 min. They observed that higher temperatures increased the selectivity toward C_1–C_4 products, while the formation of C_5–C_{10} and C_{11}–C_{25} (corresponding to the LF and HF in the lumped model of this study) became less favored. Mastral et al. (2002) performed HDPE pyrolysis in an FBR at 650–850 °C and found that the total yield of wax and oil decreased from 68.5 to 12.2 %, whereas gas production increased from 31.5 to 64.5 %. A similar

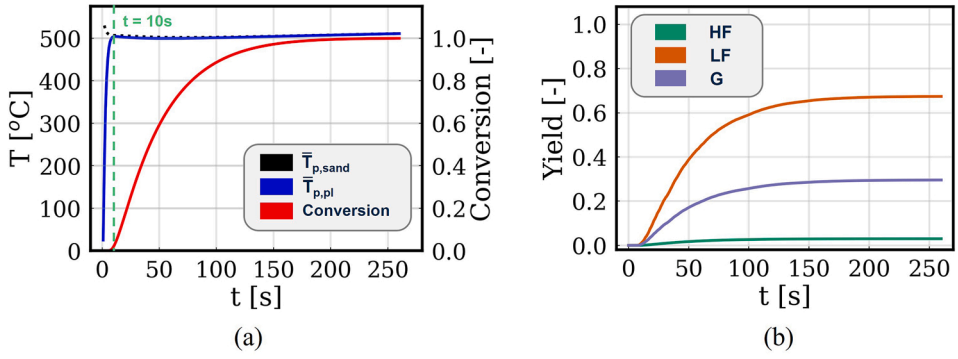

Fig. 6. Time evolution of (a) reactor and particle temperature, conversion progress and (b) product yields at 505 °C.

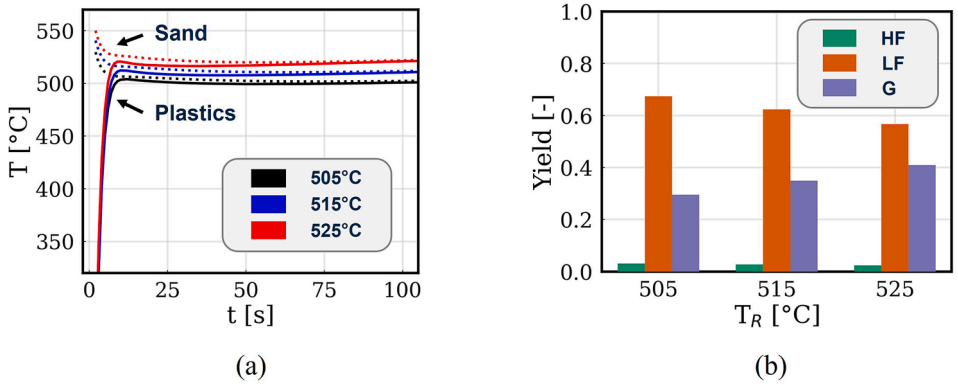

Fig. 7. Influence of reactor temperature on (a) heating behavior and (b) product yields.

variation in gas and liquid yields was also reported by Elordi et al. (2011).

4.2.2. Influence of plastic particle diameter

The second investigated parameter is the plastic particle diameter $d_{p,pl}$, which is varied from 1.5 to 2.5 mm. As illustrated in Fig. 8(a), increasing particle size prolongs the average heating time from approximately 9 to 14 s, primarily due to the attenuated external heat transfer resulting from the reduced (volume) specific surface area of larger particles. However, the pyrolysis reaction is the slower than external heat transfer under the present conditions (Py_{II} = 3.94–10.94) and occurs at nearly the same temperature for all cases. Therefore, heat transfer has a negligible impact on the product yields, which remain almost identical, as shown in Fig. 8(b).

In industrial practice, using smaller particles requires higher mechanical energy during shredding. However, this has little influence on the product yield under the investigated operating temperature. At elevated temperatures, where the timescale of convective heat transfer becomes comparable to that of the pyrolysis reactions, the enhanced heat transfer associated with smaller particles is expected to have a more pronounced impact on the yield of desired products. For reference, using the current kinetic model with Nu = 8 and $d_{p,pl}$ = 2 mm, Py_{II} drops to 0.34 at 590 °C and 0.12 at 620 °C. The latter condition falls already within the external-heat-transfer-controlled regime.

4.2.3. Influence of operation mode

As outlined in the introduction, effective plastic waste management requires high-throughput processes, which in turn necessitates continuous feeding. This consideration naturally leads to the question of whether the operation mode influences the product yields.

4.2.3.1. Batch-wise feeding. The results presented earlier were obtained under batch-wise feeding. To better capture the evolution of particle thermal states during degradation, the results from Section 4.2.1 are reanalyzed by plotting the average plastic particle temperature, $\overline{T}_{p,pl}$, against the conversion X, as shown in Fig. 9. A temperature drop of approximately $\Delta\overline{T}_{p,pl}$ = 4.5 °C was observed. This unsteady behavior arises from the endothermic nature of the pyrolysis reaction. Since the only heat source is the fluidizing gas, which has a heat capacity comparable to that of the plastics but a much lower density, the heat demand temporarily exceeds the heat supply. As previously discussed, temperature strongly influences product yields. Therefore, this temperature

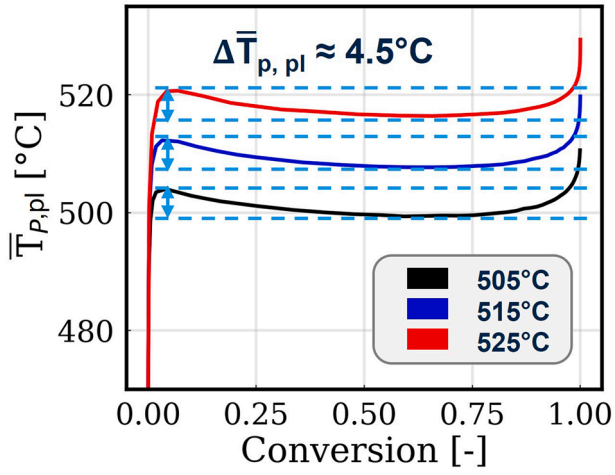

Fig. 9. Average plastic particle temperature versus conversion at T_R = 505–525 °C.

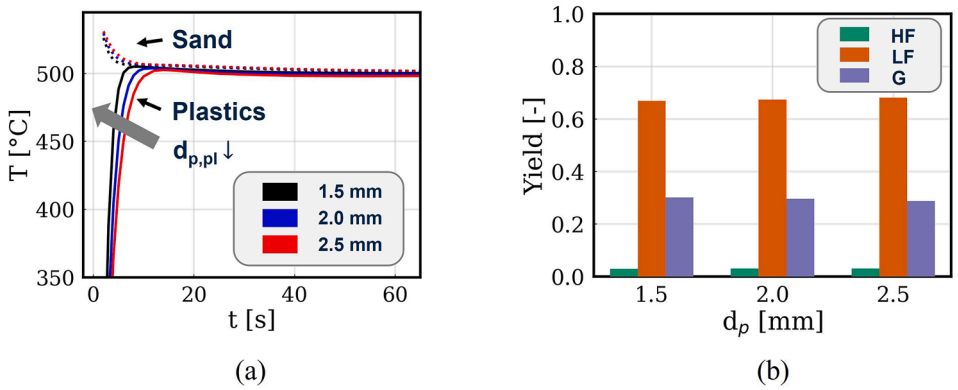

Fig. 8. Influence of plastic particle size on (a) heating behavior and (b) product yields.

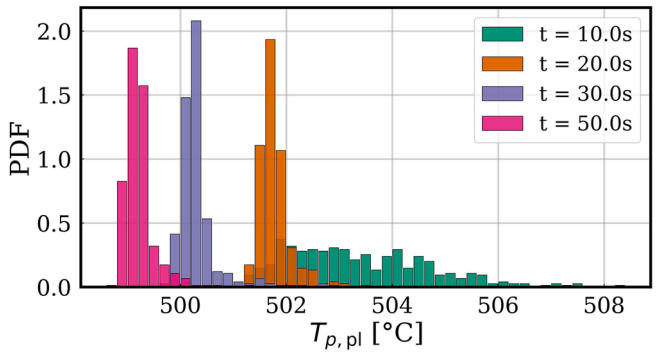

Fig. 10. Particle-scale heterogeneity in the temperature distribution of plastic particles under batch-wise feeding at T_R = 505 °C and $d_{p,pl}$ = 2 mm; bin width: 0.2 °C.

drop leads to deviations of the yields from expected values.

In addition to the average particle temperature, the temperature distribution among the plastic particles at T_R = 505 °C is also analyzed (Fig. 10). At t = 10 s, the average temperature reaches a steady value (Fig. 6(a)). However, the ensemble of plastic particles remains thermally inhomogeneous, exhibiting a temperature variation of approximately 15 °C, which becomes uniform after about 50 s. This reflects the distinct heating histories of plastic particles during the initial stage, as observed in Fig. 5. For instance, at t = 3 s, some particles remain in cooler regions (blue region, ~ 495 °C) while others are in hotter regions (red region, ~ 540 °C). Although the gas phase becomes nearly homogeneous within 10 s, the plastic particles require a longer time to reach thermal uniformity due to their higher mass and, consequently, greater thermal inertia. Furthermore, after 10 s, part of the plastic reaches around 500 °C, at which point the pyrolysis reaction begins to introduce additional thermal effects, influencing the homogenization process.

4.2.3.2. Continuous feeding. The results under continuous feeding are illustrated in Fig. 11. During the first 100 s, the mass loading of plastics is lower than the expected steady-state value. Consequently, the supplied heat exceeds the heat demand. The excess heat accumulates in the reactor and raises the reactor temperature. As the plastic mass loading (y_p) gradually increases, heat supply and demand approach an equilibrium, and the reactor stabilizes at the steady-state temperature, as shown in Fig. 11(a).

To examine the particle-scale behavior under continuous feeding, the heat-up processes of four plastic particles introduced under steady state at T_R = 505 °C is analyzed, as shown in Fig. 11(b). In contrast to the highly dispersed temperature distribution observed during the initial stage under batch-wise feeding, all four particles exhibit nearly identical heating histories from the beginning. The small temperature fluctuations observed after 10 s are due to the temporary residence near the gas inlet region, where the gas is approximately 100 °C hotter than the reactor. Consequently, the particles experience short periods of heating near the inlet, followed by cooling upon returning to the bulk region of the bed.

The above analysis demonstrates the differences in particle thermal histories under the two operation modes. In the following section, detailed statistical analyses are presented to quantitatively compare the particle heating behavior and conversion, followed by the comparison of product yields.

4.2.3.3. Comparison. To quantitatively compare the heating and degradation of the plastic particles, the coefficient of variation (CV) of plastic particle temperatures ($T_{p,pl}$) and conversions (X) of both simulations (T_R = 505 °C) is calculated following (Fitch et al., 2015):

$$CV = \frac{\sigma}{\mu} \times 100\ \%, \tag{29}$$

where σ and μ denote the standard deviation and mean value of T_p or X, respectively. The CV serves as a quantitative measure of the heterogeneity among the particles.

For the continuous feeding case, plastic particles fed during t = 200–250 s (already in steady state) are sampled. To compare the two operation modes, the CVs of $T_{p,pl}$ and X are calculated at 15–20 uniformly spaced points over the particle residence time of 0–150 s.

The results are presented in Fig. 12. Under batch-wise feeding, particle temperatures (see Fig. 12(a)) exhibit pronounced heterogeneity (up to 24 %) at the beginning, consistent with the observations in Fig. 10. In contrast, continuous feeding exhibits substantially lower thermal heterogeneity (maximum 2 %) in the initial stage. After approximately 10 s, however, CVs in both cases gradually decrease and eventually stabilize below 1 %. This is due to the batch-wise feeding introducing pulse-like perturbations into the system, which require a longer time to dissipate. The low heterogeneity after 20 s highlights the excellent heat transfer performance of the FBR.

The heterogeneity in plastic particle conversion is illustrated in Fig. 12(b). In contrast to the particle temperature, the CVs of conversion increases over time under both operation modes. However, the rate of increase gradually slows down, and the final CV remains below 5 %. This trend is attributable to conversion representing the time integral of the reaction rate, which is exponential to particle temperature. Consequently, temperature non-uniformities are cumulative, becoming reflected in the conversion distribution over time. The deceleration of the increase in conversion heterogeneity is primarily due to the decrease in temperature heterogeneity and, indirectly, to the "buffering effect" of the endothermic reaction: particles at higher temperatures react more

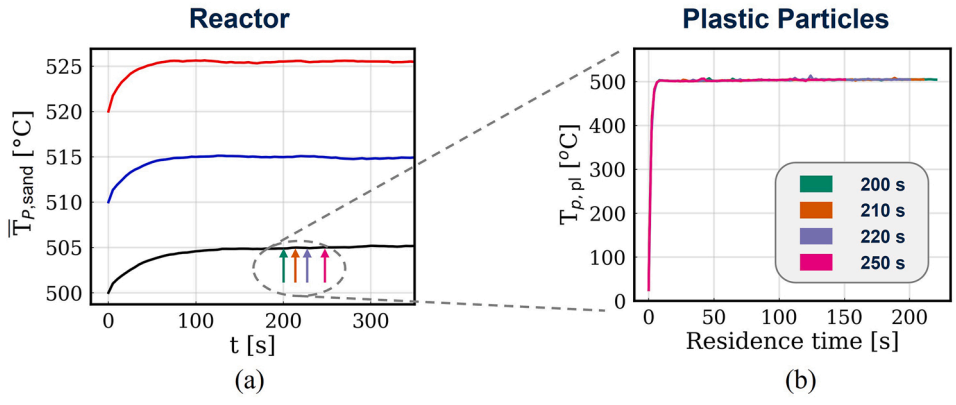

Fig. 11. Thermal steady-state and particle-scale temperature uniformity under continuous feeding: (a) reactor temperature evolution and (b) temperature profiles of plastic particles fed at different times.

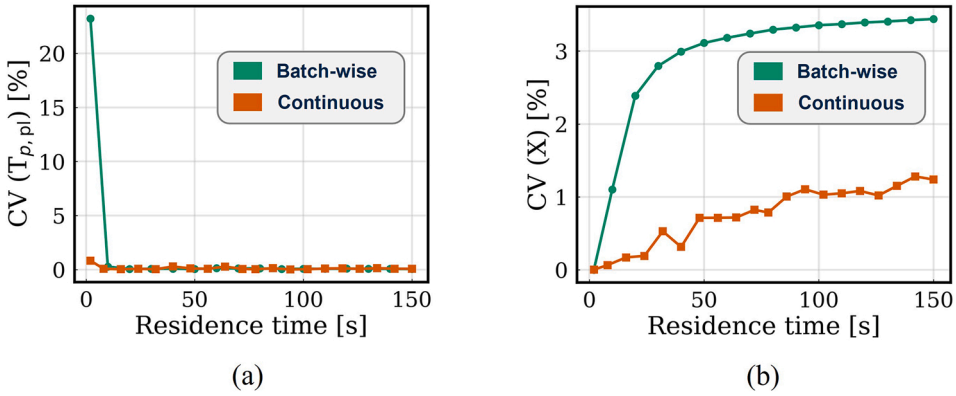

Fig. 12. Comparison of plastic particle heterogeneity under batch-wise and continuous feeding at 505 °C: (a) coefficient of variation (CV) of plastic particle temperature and (b) CV of particle conversion.

rapidly and absorb more heat, while cooler particles react more slowly, thereby diminishing the temperature discrepancies among them.

Overall, the relatively low magnitude of conversion heterogeneity again confirms that the pyrolysis reaction has a larger characteristic timescale than external heat transfer under the present conditions. The longer characteristic timescale of the chemical reaction implies that the transient temperature non-uniformity observed during the first 10 s exerts only a minor influence on the overall reaction progress. A similar trend is observed in the product yields, as shown in Fig. 13. The yields of HF, LF and G under both operation modes are comparable, differing by only approximately 2 %.

We conclude that the distinct initial thermal histories of the two operation modes, including the greater particle-scale heterogeneity seen in batch-wise feeding, have only a minor effect on product yield, as pyrolysis remains slower than external heat transfer. However, it is expected that if elevated reactor temperatures or increased non-idealities of the reactor cause Py_{II} to drop below 1 or 0.1, the impact of operating modes will become highly significant, as discussed in Section 4.2.2.

4.3. Discussion

Simulating plastic pyrolysis in FBRs involves complex, multiscale physicochemical phenomena that cannot be fully resolved due to excessive computational demands. Consequently, serval assumptions and model simplifications were adopted in Section 2 to maintain a manageable computational cost. This section assesses the impact of uncertainties associated with the modeling strategies on the simulation results.

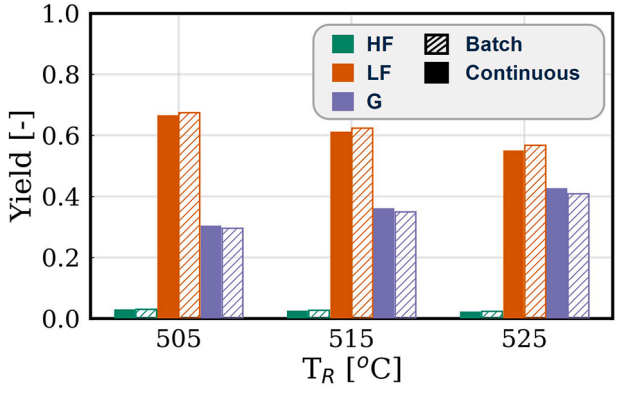

Fig. 13. Comparison of product yield under batch-wise and continuously feeding at different operating temperatures.

- **Intraparticle heat conduction**: Due to the low thermal conductivity of plastics, the conventional implementation of thermally homogeneous particle under Lagrangian framework is assessed with help of the Biot number ($Bi = hR/\lambda_p$) (Pyle & Zaror, 1984), where λ_p the thermal conductivity of PP. The Bi represents the ratio of the characteristic timescales of internal (conductive) to external (convective) heat transfer. For $d_{p,pl} = 2$ mm, the calculated Biot numbers ($Bi = 2.52$–2.61) at $T_R = 505$, 515, and 525 °C indicates slower internal conduction than external convection, as summarized in Table 5. To further evaluate the impact of conduction, additional simulations using single homogeneous-particle (0D) and particle-resolved (1D) models (Zhang, Li, et al., 2026) have been conducted, assuming an averaged Nu at 8, derived from the FBR simulations. The 1D model explicitly assess the effect of intraparticle heat conduction on pyrolysis conversion by resolving the spatial temperature gradient within the particle. As illustrated in Fig. 14(a) and (b) for $d_{p,pl} = 2$ mm and $T_R = 505$ °C, the 0D model successfully reproduces the temperature and conversion predictions from the CFD simulation, while the 1D model yields slightly slower heating and conversion due to the intraparticle thermal resistance. The same trend can be observed across all investigated temperatures ($T_R = 505$, 515, and 525 °C), as shown in Fig. 14(c) and (d). However, due to the relatively slow pyrolysis reactions (as indicated by the Py_{II} numbers evaluated in Section 4), the root-mean-square error (RMSE) for conversion (X) between the 0D and 1D predictions remains small for all cases (approx. 5 %), as shown in Table 5.

- **Simulation setup**: Furthermore, as detailed in Section 3.1, a quasi-2D computational domain has been utilized, which is simplified from a full 3D cylindrical geometry. While the simulation results has been successfully validated against experimental hydrodynamic measurements, this simplification may enhance transport processes due to the suppression of gas velocity components in the third dimension and unrealistic particle interactions and collisions with the symmetry planes. The limitation of such geometry simplification was also reported for single- and multi-particle plastic pyrolysis, where the 2D simulation underestimate the mass and heat transfer by approximately 30 % (Abdelsamie & Thévenin, 2025).
- **Eulerian–Lagrangian approach**: As mentioned in Section 2.1, the current solver neglects the fluid volume displaced by particles in the Eulerian equations ($\epsilon \approx 1$). To assess its effect, the results of current solver have been compared against the standard `MPPICFoam`, which includes ϵ in the gas-phase balances. A comparison of the instantaneous and time-averaged ϵ exhibits that our solver successfully captures the key macroscopic hydrodynamics (i.e., gas–solid circulation and core–annulus structure). However, because the gas phase equations are integrated over the entire cell volume rather than the

Table 5
Summary of 0D and 1D model predictions at different reactor temperatures.

Case	Bi	$T_{p,\text{transient}}$, RMSE [K], (0–25 s)	$T_{p,\text{transient}}$, RMSE [K], (30 s–end)	X, RMSE [%]
$T_R = 505$ °C, Nu = 8	2.52	27.59	1.26	3.39
$T_R = 515$ °C, Nu = 8	2.56	28.29	1.63	4.22
$T_R = 525$ °C, Nu = 8	2.61	28.98	2.08	5.19

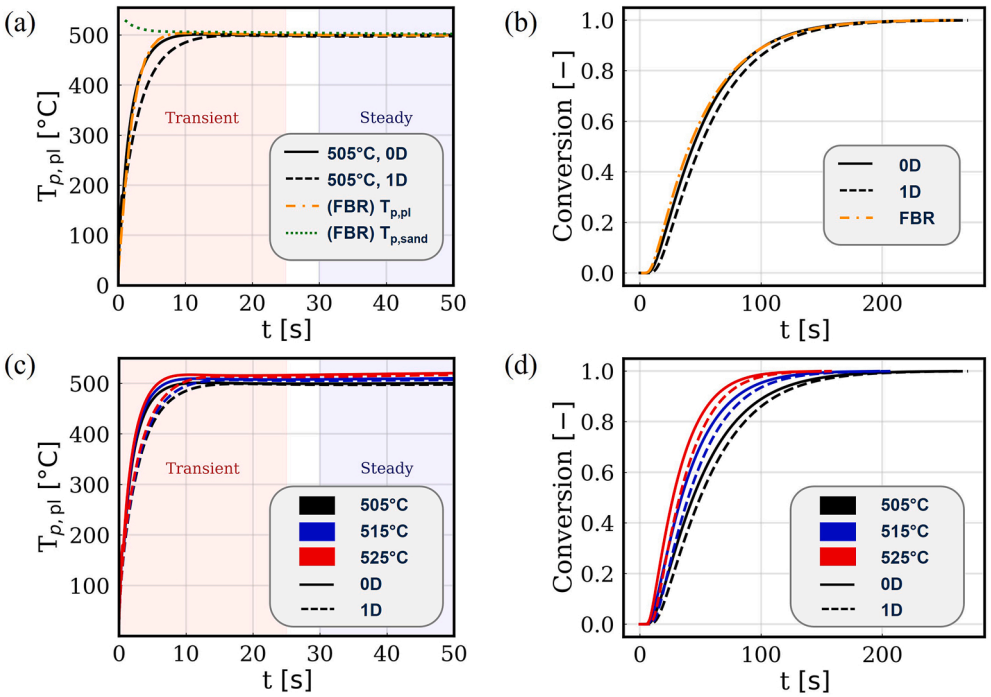

Fig. 14. Comparison of 0D and 1D model predictions for particle temperature and conversion at $d_{p,\text{pl}} = 2$ mm and $T_R = 505$, 515, and 525 °C.

interstitial space, omitting ϵ leads to enhanced gas bypassing, larger bubble formation, and greater bed expansion. These exaggerated hydrodynamic fluctuations reduce gas–solid contact, which can ultimately limit particle heating and decelerate pyrolysis rates.

- **Reaction kinetic model**: To implement the applied kinetic model (Lechleitner et al., 2020) into our multiphase simulation, several adaptations and assumptions are necessary (detailed in Section 2), which could introduce deviation in model predictions. First, the Arrhenius parameters of this lumped kinetic model were originally fitted to laboratory-scale reactor data, in which heat- and mass-transfer limitations are inevitably present. Applying these apparent kinetic parameters into our CFD simulations, which explicitly resolves convective transport, can effectively overestimates the external transfer resistance. Second, the simplified phase partitioning mentioned in Section 2.3 retains more mass on the particles and therefore underestimate the conversion. Third, as noted at the beginning of Section 2, the current work does not account for the fragmentation and crumbling of molten plastic particles. In reality, these physical phenomena would significantly increase the specific surface area and thereby accelerate the conversion of plastics.

5. Conclusion

The current work presents a Eulerian–Lagrangian solver, considering gas–particle dynamics, particle-level heat transfer and chemical reactions, as well as their mutual interactions. This solver was subsequently applied to the simulations of plastic pyrolysis in a laboratory-scale FBR, where different reactor temperatures, plastic particle sizes, and operation modes (batch-wise and continuous) were investigated to evaluate their influences on product yields from PP pyrolysis.

The results indicate that, due to bubble dynamics, the fluidized bed exhibits excellent mixing and heat-transfer performance. During PP pyrolysis at 505 °C, the LF was identified as the main product, with a yield of 67.4 wt%. Increasing the reactor temperature to 525 °C resulted in a pronounced decrease in LF yield (from 67.4 to 56.7 wt%). Furthermore, the investigation of particle size and operation mode showed that both parameters influence the thermal state of plastic particles: the former accelerates particle heating, while the latter leads to less homogeneity during the initial heating period (first 10 s). However, since the pyrolysis reactions exhibit relative longer timescale than convective heat transfer under the investigated conditions, both parameters exert only minor effects on the final product distribution.

In future work, a more detailed reaction kinetic model will be integrated, incorporating not only the boiling points of the pseudo-species but also the PIONA (n-paraffins, iso-paraffins, olefins, naphthenes and aromatics) composition of each distillation cut. This information is a key indicator in the petrochemical industry and is crucial for evaluating the downstream utilization potential of pyrolysis products.

CRediT authorship contribution statement

Muhao Li: Writing – original draft, Visualization, Validation, Software, Methodology, Investigation, Data curation, Conceptualization. **Feichi Zhang:** Writing – review & editing, Supervision, Resources, Project administration, Methodology, Conceptualization. **Thorsten Zirwes:** Writing – review & editing, Software. **Oliver T. Stein:** Writing – review & editing, Resources. **Salar Tavakkol:** Writing – review & editing, Supervision, Software, Project administration, Methodology, Funding acquisition. **Dieter Stapf:** Writing – review & editing, Supervision, Resources, Project administration, Funding acquisition.

Declaration of competing interest

The authors declare that they have no known competing financial interests or personal relationships that could have appeared to influence the work reported in this paper.

Acknowledgments

The authors gratefully acknowledge the financial support by the Helmholtz Association of German Research Centers (HGF), within the research program Materials and Technologies for the Energy Transition (MTET), topic Resource and Energy Efficiency. This work utilizes computing resources from the supercomputer HoreKa at the Scientific Centre for Computing (SCC) at KIT, Germany.

References

Abdelsamie, A., & Thévenin, D. (2025). Flow analysis and thermochemical insight during supercritical water gasification of polypropylene particles. *Physics of Fluids, 37*(12), Article 123336. https://doi.org/10.1063/5.0301174

Alobaid, F., Almohammed, N., Farid, M. M., May, J., Rößger, P., Richter, A., & Epple, B. (2022). Progress in CFD simulations of fluidized beds for chemical and energy process engineering. *Progress in Energy and Combustion Science, 91*, Article 100930. https://doi.org/10.1016/j.pecs.2021.100930

Andrews, M. J., & O'Rourke, P. J. (1996). The multiphase particle-in-cell (mp-pic) method for dense particulate flows. *International Journal of Multiphase Flow, 22*(2), 379–402. https://doi.org/10.1016/0301-9322(95)00072-0

Artetxe, M., Lopez, G., Amutio, M., Barbarias, I., Arregi, A., Aguado, R., Bilbao, J., & Olazar, M. (2015). Styrene recovery from polystyrene by flash pyrolysis in a conical spouted bed reactor. *Waste Management, 45*, 126–133. https://doi.org/10.1016/j.wasman.2015.05.034

Artetxe, M., Lopez, G., Amutio, M., Elordi, G., Bilbao, J., & Olazar, M. (2012). Light olefins from HDPE cracking in a two-step thermal and catalytic process. *Chemical Engineering Journal, 207*, 27–34. https://doi.org/10.1016/j.cej.2012.06.105

Bockhorn, H., Hornung, A., & Hornung, U. (1999). Mechanisms and kinetics of thermal decomposition of plastics from isothermal and dynamic measurements. *Journal of Analytical and Applied Pyrolysis, 50*(2), 77–101. https://doi.org/10.1016/S0165-2370(99)00026-1

Bockhorn, H., Hornung, A., Hornung, U., & Schawaller, D. (1999). Kinetic study on the thermal degradation of polypropylene and polyethylene. *Journal of Analytical and Applied Pyrolysis, 48*(2), 93–109. https://doi.org/10.1016/S0165-2370(98)00131-4

Dai, L., Zhou, N., Lv, Y., Cheng, Y., Wang, Y., Liu, Y., Cobb, K., Chen, P., Lei, H., & Ruan, R. (2022). Pyrolysis technology for plastic waste recycling: A state-of-the-art review. *Progress in Energy and Combustion Science, 93*, Article 101021. https://doi.org/10.1016/j.pecs.2022.101021

De la Flor-Barriga, L. A., & Rodríguez-Zúñiga, U. F. (2022). Numerical analysis on a catalytic pyrolysis reactor design for plastic waste upcycling using CFD modelling. *RSC Advances, 12*(20), 12436–12445. https://doi.org/10.1039/D2RA01407F

de Oliveira, L. P., Hudebine, D., Guillaume, D., & Verstraete, J. J. (2016). A review of kinetic modeling methodologies for complex processes. *Oil & Gas Science and Technology–Revue d'IFP Energies nouvelles, 71*(3), 45. https://doi.org/10.2516/ogst/2016011

Ding, K., Xiong, Q., Zhong, Z., Zhong, D., & Zhang, Y. (2020). CFD simulation of combustible solid waste pyrolysis in a fluidized bed reactor. *Powder Technology, 362*, 177–187. https://doi.org/10.1016/j.powtec.2019.12.011

Dogu, O., Pelucchi, M., Van de Vijver, R., Van Steenberge, P. H., D'hooge, D. R., Cuoci, A., Mehl, M., Frassoldati, A., Faravelli, T., & Van Geem, K. M. (2021). The chemistry of chemical recycling of solid plastic waste via pyrolysis and gasification: State-of-the-art, challenges, and future directions. *Progress in Energy and Combustion Science, 84*, Article 100901. https://doi.org/10.1016/j.pecs.2020.100901

Donaj, P. J., Kaminsky, W., Buzeto, F., & Yang, W. (2012). Pyrolysis of polyolefins for increasing the yield of monomers' recovery. *Waste Management, 32*(5), 840–846. https://doi.org/10.1016/j.wasman.2011.10.009

Durupt, N., Aoulmi, A., Bouroukba, M., & Rogalski, M. (1996). Heat capacities of liquid long-chain alkanes. *Thermochimica Acta, 274*, 73–80. https://doi.org/10.1016/0040-6031(95)02255-4

Elordi, G., Olazar, M., Lopez, G., Amutio, M., Artetxe, M., Aguado, R., & Bilbao, J. (2009). Catalytic pyrolysis of HDPE in continuous mode over zeolite catalysts in a conical spouted bed reactor. *Journal of Analytical and Applied Pyrolysis, 85*(1–2), 345–351. https://doi.org/10.1016/j.jaap.2008.10.015

Elordi, G., Olazar, M., Lopez, G., Artetxe, M., & Bilbao, J. (2011). Product yields and compositions in the continuous pyrolysis of high-density polyethylene in a conical spouted bed reactor. *Industrial & Engineering Chemistry Research, 50*(11), 6650–6659. https://doi.org/10.1021/ie200186m

Fitch, P. J., Lovell, M. A., Davies, S. J., Pritchard, T., & Harvey, P. K. (2015). An integrated and quantitative approach to petrophysical heterogeneity. *Marine and Petroleum Geology, 63*, 82–96. https://doi.org/10.1016/j.marpetgeo.2015.02.014

Gidaspow, D. (1994). *Multiphase flow and fluidization: Continuum and kinetic theory descriptions*. San Diego, California: Academic Press.

Grace, J. R., Bi, X., & Ellis, N. (2020). *Essentials of fluidization technology*. John Wiley & Sons.

Gunn, D. (1978). Transfer of heat or mass to particles in fixed and fluidised beds. *International Journal of Heat and Mass Transfer, 21*(4), 467–476. https://doi.org/10.1016/0017-9310(78)90080-7

Harris, S., & Crighton, D. (1994). Solitons, solitary waves, and voidage disturbances in gas-fluidized beds. *Journal of Fluid Mechanics, 266*, 243–276. https://doi.org/10.1017/S0022112094000996

Kaminsky, W. (2021). Chemical recycling of plastics by fluidized bed pyrolysis. *Fuel Communications, 8*, Article 100023. https://doi.org/10.1016/j.jfueco.2021.100023

Kaminsky, W., Predel, M., & Sadiki, A. (2004). Feedstock recycling of polymers by pyrolysis in a fluidised bed. *Polymer Degradation and Stability, 85*(3), 1045–1050. https://doi.org/10.1016/j.polymdegradstab.2003.05.002

Kusenberg, M., Eschenbacher, A., Delva, L., De Meester, S., Delikonstantis, E., Stefanidis, G. D., Ragaert, K., & Van Geem, K. M. (2022). Towards high-quality petrochemical feedstocks from mixed plastic packaging waste via advanced recycling: The past, present and future. *Fuel Processing Technology, 238*, Article 107474. https://doi.org/10.1016/j.fuproc.2022.107474

Lechleitner, A. E., Schubert, T., Hofer, W., & Lehner, M. (2020). Lumped kinetic modeling of polypropylene and polyethylene co-pyrolysis in tubular reactors. *Processes, 9*(1), 34. https://doi.org/10.3390/pr9010034

Lopez, G., Artetxe, M., Amutio, M., Bilbao, J., & Olazar, M. (2017). Thermochemical routes for the valorization of waste polyolefinic plastics to produce fuels and chemicals. a review. *Renewable and Sustainable Energy Reviews, 73*, 346–368. https://doi.org/10.1016/j.rser.2017.01.142

Madorsky, S. L. (1952). Rates of thermal degradation of polystyrene and polyethylene in a vacuum. *Journal of Polymer Science, 9*(2), 133–156. https://doi.org/10.1002/pol.1952.120090203

Madorsky, S. (1953). Rates and activation energies of thermal degradation of styrene and acrylate polymers in a vacuum. *Journal of Polymer Science, 11*(5), 491–506. https://doi.org/10.1002/pol.1953.120110511

Mastral, F., Esperanza, E., Garcıa, P., & Juste, M. (2002). Pyrolysis of high-density polyethylene in a fluidised bed reactor. influence of the temperature and residence time. *Journal of Analytical and Applied Pyrolysis, 63*(1), 1–15. https://doi.org/10.1016/S0165-2370(01)00137-1

Mazloum, S., Awad, S., Allam, N., Aboumsallem, Y., Loubar, K., & Tazerout, M. (2021). Modelling plastic heating and melting in a semi-batch pyrolysis reactor. *Applied Energy, 283*, Article 116375. https://doi.org/10.1016/j.apenergy.2020.116375

Merkel, A., Plessing, L., Luinstra, G. A., Gruenewald, M., & Biessey, P. (2023). Development of a separation sequence for the integration of a styrene recyclate into polystyrene production. *Chemie Ingenieur Technik, 95*(8), 1323–1331. https://doi.org/10.1002/cite.202100210

Netsch, N., Vogt, J., Richter, F., Straczewski, G., Mannebach, G., Fraaije, V., Tavakkol, S., Mihan, S., & Stapf, D. (2023). Chemical recycling of polyolefinic waste to light olefins by catalytic pyrolysis. *Chemie Ingenieur Technik, 95*(8), 1305–1313. https://doi.org/10.1002/cite.202300078

Netsch, N., Zeller, M., Richter, F., Bergfeldt, B., Tavakkol, S., & Stapf, D. (2024). Energy demand for pyrolysis of mixed thermoplastics and waste plastics in chemical recycling: Model prediction and pilot-scale validation. *ACS Sustainable Resource Management, 1*(7), 1485–1492. https://doi.org/10.1021/acssusresmgt.4c00109

OECD. (2022). *Global plastics outlook: Policy scenarios to 2060*. Paris: OECD Publishing. https://doi.org/10.1787/aa1edf33-en

Oka, S. (2004). *Fluidized bed combustion*. New York: Marcel Dekker, Inc.

Pyle, D. L., & Zaror, C. A. (1984). Heat transfer and kinetics in the low temperature pyrolysis of solids. *Chemical Engineering Science, 39*(1), 147–158. https://doi.org/10.1016/0009-2509(84)80140-2

Shen, J., Dai, J., Gao, S., Ma, Z., Li, S., Patrascu, M., & Gao, X. (2025). Multiscale modeling of plastic pyrolysis in a fluidized pyrolyzer with NN-inspired kinetics and experimental validation. *ACS Sustainable Chemistry & Engineering*. https://doi.org/10.1021/acssuschemeng.5c04293

Shen, J., Dai, J., Lin, H., Li, S., Gao, S., Cheng, Y., Patrascu, M., & Gao, X. (2024). Multiscale modeling of plastic pyrolysis with a neural network-inspired pyrolysis kinetic model and coarse-grained dem-cfd. *Industrial & Engineering Chemistry Research, 63*(28), 12688–12703. https://doi.org/10.1021/acs.iecr.4c01882

Tavakkol, S., Zirwes, T., Denev, J. A., Jamshidi, F., Weber, N., Bockhorn, H., & Trimis, D. (2021). An eulerian-lagrangian method for wet biomass carbonization in rotary kiln reactors. *Renewable and Sustainable Energy Reviews, 139*, Article 110582. https://doi.org/10.1016/j.rser.2020.110582

van Wyk, S., Vilela, C. F. M., Meijwes, C., Geusebroek, M., & Toonen, A. (2026). Thermal cracking of polyolefin waste: Primary and secondary product formation as a function of gas phase residence time in bubbling fluidized bed. *Fuel, 407*, Article 137561. https://doi.org/10.1016/j.fuel.2025.137561

Wong, H.-W., & Broadbelt, L. J. (2001). Tertiary resource recovery from waste polymers via pyrolysis: Neat and binary mixture reactions of polypropylene and polystyrene. *Industrial & Engineering Chemistry Research, 40*(22), 4716–4723. https://doi.org/10.1021/ie010171s

Zhang, F., Dai, X., Li, M., Tavakkol, S., & Stapf, D. (2026). Numerical analysis of hydrodynamics in conical spouted bed reactors. *Physics of Fluids, 38*(5), Article 053333. https://doi.org/10.1063/5.0327700

Zhang, F., Li, M., Ma, X., Netsch, N., Tavakkol, S., Zirwes, T., Zhang, R., & Stapf, D. (2026). Assessment of the interplay between convective heat transfer and reaction

kinetics during plastic pyrolysis. *Particuology, 113*, 180–188. https://doi.org/10.1016/j.partic.2026.03.019

Zhang, F., Tavakkol, S., Dercho, S., Zhou, J., Zirwes, T., Zeller, M., Vogt, J., Zhang, R., Bockhorn, H., & Stapf, D. (2024). Assessment of dynamic characteristics of fluidized beds via numerical simulations. *Physics of Fluids, 36*(2). https://doi.org/10.1063/5.0189519

Zhang, F., Tavakkol, S., Galeazzo, F. C., & Stapf, D. (2025). Particle-resolved simulation of the pyrolysis process of a single plastic particle. *Heat and Mass Transfer, 61*(1), 12. https://doi.org/10.1007/s00231-024-03524-6